ELSEVIER

J. Non-Newtonian Fluid Mech. 129 (2005) 106–116

Journal of Non-Newtonian Fluid Mechanics

www.elsevier.com/locate/jnnfm

Purely irrotational theories of the effects of viscosity and viscoelasticity on capillary instability of a liquid cylinder

J. Wang[a], D.D. Joseph[a,*], T. Funada[b]

[a] *Department of Aerospace Engineering and Mechanics, University of Minnesota, 110 Union St. SE, Minneapolis, MN 55455, USA*
[b] *Department of Digital Engineering, Numazu College of Technology, 3600 Ooka, Numazu, Shizuoka 410-8501, Japan*

Received 23 September 2004; received in revised form 19 March 2005; accepted 20 April 2005

Abstract

Capillary instability of a liquid cylinder can arise when either the interior or exterior fluid is a gas of negligible density and viscosity. The shear stress must vanish at the gas-liquid interface but it does not vanish in irrotational flows. Joseph and Wang [D.D. Joseph, J. Wang, The dissipation approximation and viscous potential flow, J. Fluid Mech. 505 (2004) 365] derived an additional viscous correction to the irrotational pressure. They argued that this pressure arises in a boundary layer induced by the unphysical discontinuity of the shear stress. Wang et al. [J. Wang, D.D. Joseph, T. Funada, Pressure correction for potential flow analysis of capillary instability of viscous fluids, J. Fluid Mech. 522 (2005) 383] showed that the dispersion relation for capillary instability in the Newtonian case is almost indistinguishable from the exact solution when the additional pressure contribution is included in the irrotational theory. Here we extend the formulation for the additional pressure to potential flows of viscoelastic fluids in flows governed by linearized equations, and apply this additional pressure to capillary instability of viscoelastic liquid filaments of Jeffreys type. The shear stress at the gas–liquid interface cannot be made to vanish in an irrotational theory, but the explicit effect of this uncompensated shear stress can be removed from the global equation for the evolution of the energy of disturbances. This line of thought allows us to present the additional pressure theory without appeal to boundary layers. The validity of this purely irrotational theory can be judged by comparison with the exact solutions of Navier–Stokes equations. Here we show that our purely irrotational theory is in remarkably good agreement with the exact solution in linear analysis of the capillary instability of a viscoelastic liquid cylinder.

Keywords: Capillary instability; Viscoelastic potential flow; Additional pressure contribution; Dissipation method

1. Introduction

Capillary instability of a liquid cylinder of mean radius R leading to capillary collapse can be described as a neck-down due to surface tension γ in which fluid is ejected from the throat of the neck, leading to a smaller neck and greater neckdown capillary force as seen in the diagram in Fig. 1.

Capillary instability of Newtonian fluids was studied by Rayleigh [1] following earlier work by Plateau [2] who showed that a long cylinder of liquid is unstable to disturbances with wave lengths greater than $2\pi R$. The analysis of Rayleigh is based on potential flow of an inviscid liquid. Tomotika [3] studied the capillary instability and gave an exact normal mode solution of the linearized Navier–Stokes equations.

The linear analysis of capillary instability of viscoelastic fluids has been done by Middleman [4], Goldin et al. [5], Goren and Gottlieb [6]. They showed that the growth rates are larger for the viscoelastic fluids than for the equivalent Newtonian fluids.

Funada and Joseph [7,8] presented potential flow analyses of capillary instability of viscous and viscoelastic fluids. In their studies, the flow is assumed to be irrotational but the viscous and viscoelastic effects are retained (viscous or viscoelastic potential flow, VPF). The viscous and viscoelastic stresses enter into the analyses through the normal stress balance at the interface. Funada and Joseph compared their results based on potential flow to the unapproximated normal mode results (Tomotika [3]). They showed that the results with viscous and viscoelastic effects retained are in

* Corresponding author. Tel.: +1 612 625 0309; fax: +1 612 626 1558.
E-mail address: joseph@aem.umn.edu (D.D. Joseph).

0377-0257/$ – see front matter © 2005 Elsevier B.V. All rights reserved.
doi:10.1016/j.jnnfm.2005.04.003

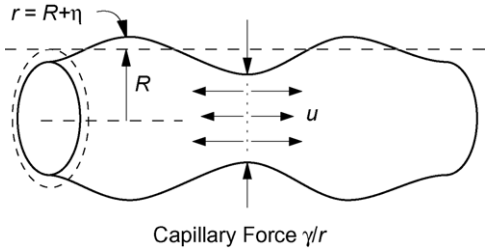

Fig. 1. Capillary instability. The force γ/r drives fluid away from the throat, leading to collapse.

better agreement with the unapproximated results than those assuming inviscid fluids.

The capillary instability can be viewed as a free surface problem when either the interior or the exterior fluid is a gas of negligible density and viscosity. One difficulty in the potential flow analyses of free surface problems is that the non-zero irrotational shear stress violates the zero-shear-stress condition at the free surface. Joseph and Wang [9] derived an additional viscous correction for the irrotational pressure, which arises in the boundary layer induced by the unphysical discontinuity of the shear stress. Wang et al. [10] applied this additional pressure contribution to the potential flow analysis of capillary instability of Newtonian fluids. They showed that the results computed with the additional pressure contribution are almost indistinguishable from the exact results. Here we extend the formulation for the additional pressure correction to potential flows of viscoelastic fluids in flows governed by linearized equations (viscoelastic correction of viscoelastic potential flow, VCVPF), and apply this additional pressure correction to capillary instability of viscoelastic liquid filaments of Jeffreys type. The results are in remarkably good agreement with those obtained from the unapproximated normal mode analysis for viscoelastic fluids.

The linear stability analysis given here and elsewhere indicates that the liquid jets are less stable with increasing elasticity, which contradicts the observation in experiments. A possible explanation of this contradiction is related to the linear stability analysis of a stressed filament at rest (Entov [11]). One difficulty is that a stressed filament at rest is not a permanent solution.

2. Linear stability equations and the exact solution (Tomotika [3])

In an undisturbed rest state, the long cylinder of a viscoelastic liquid is surrounded by a gas of negligible density and viscosity. We use cylindrical coordinates (r, θ, z) and consider small axisymmetric disturbances. The linearized governing equations of the interior liquid are

$$\nabla \cdot \boldsymbol{u} = 0, \tag{1}$$

$$\rho \frac{\partial \boldsymbol{u}}{\partial t} = -\nabla p + \nabla \cdot \boldsymbol{\tau} \tag{2}$$

where $\boldsymbol{u} = u\boldsymbol{e}_r + w\boldsymbol{e}_z$ is the velocity, ρ is the density, p is the pressure, and $\boldsymbol{\tau}$ is the extra stress. The extra stress may be modeled by Jeffreys model

$$\boldsymbol{\tau} + \lambda_1 \frac{\partial \boldsymbol{\tau}}{\partial t} = 2\mu \left(\mathbf{D} + \lambda_2 \frac{\partial \mathbf{D}}{\partial t} \right), \tag{3}$$

where $\mathbf{D}$ is the rate of strain tensor, μ is the viscosity, λ_1 and λ_2 are the relaxation and retardation times, respectively. Suppose that we have normal mode solutions with the growth rate σ:

$$\boldsymbol{\tau} = \exp(\sigma t)\tilde{\boldsymbol{\tau}} \quad \text{and} \quad \mathbf{D} = \exp(\sigma t)\tilde{\mathbf{D}}, \tag{4}$$

then (3) leads to

$$\tilde{\boldsymbol{\tau}} = \frac{1 + \lambda_2\sigma}{1 + \lambda_1\sigma} 2\mu\tilde{\mathbf{D}} \quad \Rightarrow \quad \boldsymbol{\tau} = \frac{1 + \lambda_2\sigma}{1 + \lambda_1\sigma} 2\mu\mathbf{D}. \tag{5}$$

The momentum Eq. (2) becomes

$$\begin{aligned} \rho \frac{\partial \boldsymbol{u}}{\partial t} &= -\nabla p + \nabla \cdot \left(\frac{1 + \lambda_2\sigma}{1 + \lambda_1\sigma} 2\mu\mathbf{D} \right) \\ &= -\nabla p + \frac{1 + \lambda_2\sigma}{1 + \lambda_1\sigma} \mu \nabla^2 \boldsymbol{u}. \end{aligned} \tag{6}$$

The shear and normal stress boundary conditions are

$$\frac{1 + \lambda_2\sigma}{1 + \lambda_1\sigma} \mu \left(\frac{\partial u}{\partial z} + \frac{\partial w}{\partial r} \right) = 0; \tag{7}$$

$$-p + \frac{1 + \lambda_2\sigma}{1 + \lambda_1\sigma} 2\mu \frac{\partial u}{\partial r} = \gamma \left(\frac{\partial^2 \eta}{\partial z^2} + \frac{\eta}{R^2} \right), \tag{8}$$

where η is the varicose displacement. The governing Eqs. (1) and (6) and boundary conditions (8) and (7) are the same as those for a Newtonian fluid except that $(1 + \lambda_2\sigma)\mu/(1 + \lambda_1\sigma)$ replaces μ.

Following scales are used to construct dimensionless governing equations: the cylinder diameter D for length, $U = \sqrt{\gamma/(\rho D)}$ for velocity, $T = D/U$ for time and $p_0 = \rho U^2$ for pressure. The dimensionless momentum equation is (we use the same symbols for dimensionless variables)

$$\frac{\partial \boldsymbol{u}}{\partial t} = -\nabla p + \frac{\hat{\mu}}{\sqrt{J}} \nabla^2 \boldsymbol{u}, \tag{9}$$

where

$$\hat{\mu} = \frac{1 + \hat{\lambda}_2\sigma}{1 + \hat{\lambda}_1\sigma} \tag{10}$$

with

$$\hat{\lambda}_1 = \lambda_1 \frac{U}{D} = \lambda_1 \sqrt{\frac{\gamma}{\rho D^3}} \quad \text{and} \quad \hat{\lambda}_2 = \lambda_2 \frac{U}{D} = \lambda_2 \sqrt{\frac{\gamma}{\rho D^3}}, \tag{11}$$

and

$$J = \frac{\rho\gamma D}{\mu^2} \tag{12}$$

is the Reynolds number and $J^{-1/2}$ is the Ohnesorge number. The dimensionless boundary conditions at the cylinder surface $R = 0.5$ are

$$-p + 2\frac{\hat{\mu}}{\sqrt{J}}\frac{\partial u}{\partial r} = \frac{\partial^2 \eta}{\partial z^2} + \frac{\eta}{R^2}; \tag{13}$$

$$\frac{\hat{\mu}}{\sqrt{J}}\left(\frac{\partial u}{\partial z} + \frac{\partial w}{\partial r}\right) = 0. \tag{14}$$

A solution of (9) which satisfies both the boundary conditions (13) and (14) takes the following form:

$$\psi = [A_1 r I_1(kr) + A_2 r I_1(k_v r)]\exp(\sigma t + \mathrm{i}kz), \quad u = \frac{1}{r}\frac{\partial \psi}{\partial z},$$

$$w = -\frac{1}{r}\frac{\partial \psi}{\partial r}, \tag{15}$$

$$\eta = H\exp(\sigma t + \mathrm{i}kz), \tag{16}$$

where k is the wave number and I_1 denotes the first kind modified Bessel function of the first order. Substitution of (15) and (16) into (13) and (14) leads to the solvability condition, which is given as the dispersion relation of σ:

$$\begin{vmatrix} 2k^2 I_1(kR) & (k^2 + k_v^2) I_1(k_v R) \\ F_1 & F_2 \end{vmatrix} = 0 \tag{17}$$

where

$$F_1 = \sigma I_0(kR) + 2\frac{\hat{\mu}k^2}{\sqrt{J}}\left(\frac{\mathrm{d}I_1(kR)}{\mathrm{d}(kR)}\right) - \left(\frac{1}{R^2} - k^2\right)\frac{k}{\sigma} I_1(kR), \tag{18}$$

$$F_2 = 2\frac{\hat{\mu}kk_v}{\sqrt{J}}\left(\frac{\mathrm{d}I_1(k_v R)}{\mathrm{d}(k_v R)}\right) - \left(\frac{1}{R^2} - k^2\right)\frac{k}{\sigma} I_1(k_v R), \tag{19}$$

with $k_v = \sqrt{k^2 + (\sqrt{J}/\hat{\mu})\sigma}$. This solution satisfies the governing equations and all the boundary conditions and is an exact solution.[1]

3. Viscoelastic potential flow (VPF)

It is easy to show that the momentum Eq. (9) admits potential flow solutions. Take curl of Eq. (9) and use $\boldsymbol{u} = \nabla\phi$, we obtain

$$\nabla \wedge \frac{\partial \nabla\phi}{\partial t} = \nabla \wedge (-\nabla p) + \frac{\hat{\mu}}{\sqrt{J}}\nabla \wedge \nabla^2 \nabla\phi. \tag{20}$$

Both sides of (20) are zero, therefore potential flow solutions are compatible in this problem. The pressure integral can also be easily obtained from (9),

$$\nabla\left(\frac{\partial \phi}{\partial t}\right) = -\nabla p_p + \frac{\hat{\mu}}{\sqrt{J}}\nabla\nabla^2\phi \Rightarrow p_p = -\frac{\partial \phi}{\partial t}, \tag{21}$$

where p_p denotes the pressure from the potential flow solution and it is equal to the pressure from the inviscid potential flow.

The potential flow solution is given by

$$\phi = A\mathrm{i}I_0(kr)\exp(\sigma t + \mathrm{i}kz), \quad u = \frac{\partial \phi}{\partial r}, \quad w = \frac{\partial \phi}{\partial z}, \tag{22}$$

$$\eta = H\exp(\sigma t + \mathrm{i}kz). \tag{23}$$

Substitution of the potential flow solution into the normal stress balance (13) leads to the dispersion relation

$$\frac{I_0(kR)}{I_1(kR)}\sigma^2\left(1 + \hat{\lambda}_1\sigma\right) + \left(1 + \hat{\lambda}_2\sigma\right)\sigma\frac{2k^2}{\sqrt{J}}\left[\frac{I_0(kR)}{I_1(kR)} - \frac{1}{kR}\right] - k\left(\frac{1}{R^2} - k^2\right)\left(1 + \hat{\lambda}_1\sigma\right) = 0, \tag{24}$$

which is a cubic equation of σ and has explicit solutions.

When $J \to \infty$, Eq. (24) reduces to

$$\frac{I_0(kR)}{I_1(kR)}\sigma^2 = k\left(\frac{1}{R^2} - k^2\right), \tag{25}$$

which is the dispersion relation for inviscid potential flow (IPF) solution. The IPF solution does not allow viscous or viscoelastic effects.

4. Dissipation and the formulation for the additional pressure contribution

Joseph and Wang [9] derived a viscous pressure contribution in addition to the irrotational pressure for the potential flow solutions of Newtonian fluids by considering the dissipation of energy. Here we extend the analysis to a viscoelastic fluid of Jeffereys type in flows governed by linearized equations. We start from the momentum equation

$$\rho\frac{\mathrm{d}\boldsymbol{u}}{\mathrm{d}t} = \nabla\cdot\mathbf{T} \Rightarrow \boldsymbol{u}\cdot\rho\frac{\mathrm{d}\boldsymbol{u}}{\mathrm{d}t} = (\nabla\cdot\mathbf{T})\cdot\boldsymbol{u}, \tag{26}$$

where $\mathbf{T}$ is the total stress. It follows that

$$\begin{aligned}\rho\frac{\mathrm{d}}{\mathrm{d}t}\left(\frac{1}{2}\boldsymbol{u}\cdot\boldsymbol{u}\right) &= \nabla\cdot(\mathbf{T}\cdot\boldsymbol{u}) - \nabla\boldsymbol{u} : \mathbf{T} \\ &= \nabla\cdot(\mathbf{T}\cdot\boldsymbol{u}) - (\mathbf{D} + \boldsymbol{\Omega}) : (-p\mathbf{1} + 2\hat{\mu}\mu\mathbf{D}) \\ &= \nabla\cdot(\mathbf{T}\cdot\boldsymbol{u}) - \mathbf{D} : (-p\mathbf{1} + 2\hat{\mu}\mu\mathbf{D}) \\ &= \nabla\cdot(\mathbf{T}\cdot\boldsymbol{u}) - 2\hat{\mu}\mu\mathbf{D} : \mathbf{D}.\end{aligned}$$

It follows that

$$\frac{\mathrm{d}}{\mathrm{d}t}\int_V \left(\frac{\rho}{2}\boldsymbol{u}\cdot\boldsymbol{u}\right)\mathrm{d}V = \int_\Omega \boldsymbol{n}\cdot(\mathbf{T}\cdot\boldsymbol{u})\mathrm{d}\Omega - 2\hat{\mu}\mu\int_V \mathbf{D} : \mathbf{D}\,\mathrm{d}V, \tag{27}$$

[1] In our former paper [10], the exact solution of the linearized equations was called the fully viscous flow (FVF) solution.

where V is the volume occupied by the viscoelastic fluid, Ω is the boundary of V, and $\boldsymbol{n}$ is the outward normal of V on Ω. We have shown that the potential flow is a solution of the momentum equation in this problem. Thus we can insert the velocity and stress tensor evaluated on the potential flow into (27) to obtain

$$\frac{\mathrm{d}}{\mathrm{d}t}\int_V \left(\frac{\rho}{2}\boldsymbol{u}\cdot\boldsymbol{u}\right)\mathrm{d}V = \int_\Omega [(-p_p+\tau_{rr})u+\tau_{rz}w]\mathrm{d}\Omega - 2\hat{\mu}\mu\int_V \mathbf{D}:\mathbf{D}\,\mathrm{d}V. \tag{28}$$

At the free surface, the potential flow leads to a non-zero irrotational shear stress and does not satisfy the zero-shear-stress condition. We introduce a pressure contribution p_c in addition to the irrotational pressure p_p; p_c cancels out the power due to the unphysical irrotational shear stress in the energy equation and (27) becomes

$$\frac{\mathrm{d}}{\mathrm{d}t}\int_V \left(\frac{\rho}{2}\boldsymbol{u}\cdot\boldsymbol{u}\right)\mathrm{d}V = \int_\Omega [(-p_p-p_c+\tau_{rr})u]\mathrm{d}\Omega - 2\hat{\mu}\mu\int_V \mathbf{D}:\mathbf{D}\,\mathrm{d}V. \tag{29}$$

Comparing (28) and (29), we obtain

$$\int_\Omega \tau_{rz}w\mathrm{d}\Omega = \int_\Omega (-p_c)u\,\mathrm{d}\Omega, \tag{30}$$

which is the same as the formulation for the additional pressure contribution as in the potential flow of a viscous Newtonian fluid (Joseph and Wang [9]). However, the calculation of τ_{rz} in viscoelastic fluids is different than in Newtonian fluids. The additional pressure contribution p_c depends strongly on viscoelastic parameters and is determined solely by the irrotational flow.

5. The additional pressure contribution for capillary instability

Now we consider the additional pressure contribution for the potential flow analysis of capillary instability. Joseph and Wang [9] showed that in linearized problems, the governing equation for the additional pressure contribution is

$$\nabla^2 p_c = 0. \tag{31}$$

It is easy to show that (31) holds for the viscoelastic fluid under consideration here. Solving (31), we obtain

$$-p_c = \sum_{j=0}^{\infty} C_j \mathrm{i} I_0(jr)\exp(\sigma t+\mathrm{i}jz), \tag{32}$$

where C_j are constants. With the additional pressure contribution, the normal stress balance becomes

$$-p_p - p_c + 2\hat{\mu}\frac{1}{\sqrt{J}}\frac{\partial u}{\partial r} = \frac{\partial^2\eta}{\partial z^2}+\frac{\eta}{R^2}, \tag{33}$$

which gives rise to

$$\left\{A\sigma I_0(kR)+C_k I_0(kR)+\frac{2\hat{\mu}k^2}{\sqrt{J}}A\left[I_0(kR)-\frac{I_1(kR)}{kR}\right]\right\}\times\exp(\sigma t+\mathrm{i}kz)+\sum_{j\neq k}C_j I_0(jR)\exp(\sigma t+\mathrm{i}jz) = A\frac{k}{\sigma}I_1(kR)\left(\frac{1}{R^2}-k^2\right)\exp(\sigma t+\mathrm{i}kz). \tag{34}$$

By orthogonality of Fourier series, $C_j = 0$ if $j\neq k$. The coefficient C_k can be determined using (30). The left hand side of (30) is

$$\int_\Omega \tau_{rz}w^*\,\mathrm{d}\Omega = \frac{\hat{\mu}}{\sqrt{J}}4\pi l R A A^* k^3 I_0(kR)I_1(kR)\exp(\sigma+\sigma^*)t, \tag{35}$$

where l is the length of one wave period and "$*$" denotes conjugate variables. On the other hand,

$$\int_\Omega (-p_c)u^*\,\mathrm{d}\Omega = 2\pi l R C_k A^* k I_0(kR)I_1(kR)\exp(\sigma+\sigma^*)t. \tag{36}$$

It follows that $C_k = 2(\hat{\mu}/\sqrt{J})Ak^2$ and

$$-p_c = \mathrm{i}Ak^2\frac{2\hat{\mu}}{\sqrt{J}}I_0(kr)\exp(\sigma t+\mathrm{i}kz). \tag{37}$$

Inserting C_k into (34), we obtain

$$\sigma I_0(kR)+\frac{2\hat{\mu}k^2}{\sqrt{J}}I_0(kR)+\frac{2\hat{\mu}k^2}{\sqrt{J}}\left[I_0(kR)-\frac{I_1(kR)}{kR}\right] = \frac{k}{\sigma}I_1(kR)\left(\frac{1}{R^2}-k^2\right),$$

which can be written as

$$\frac{I_0(kR)}{I_1(kR)}\sigma^2\left(1+\hat{\lambda}_1\sigma\right)+\left(1+\hat{\lambda}_2\sigma\right)\sigma\frac{2k^2}{\sqrt{J}}\left[\frac{2I_0(kR)}{I_1(kR)}-\frac{1}{kR}\right] - k\left(\frac{1}{R^2}-k^2\right)\left(1+\hat{\lambda}_1\sigma\right)=0. \tag{38}$$

Eq. (38) is the dispersion relation from the viscoelastic correction of VPF (VCVPF).

If the pressure correction (37) is inserted back into the governing Eq. (9), we obtain

$$\frac{\partial \boldsymbol{u}_c}{\partial t} = -\nabla p_c + \frac{\hat{\mu}}{\sqrt{J}}\nabla^2\boldsymbol{u}_c, \tag{39}$$

where $\boldsymbol{u}_c$ is the velocity correction induced by the pressure correction p_c. We can find a potential flow solution $\boldsymbol{u}_c = \nabla\phi_c$, such that $\nabla^2\boldsymbol{u}_c = \nabla\nabla^2\phi_c = 0$ and

$$\nabla\frac{\partial}{\partial t}\phi_c = -\nabla p_c. \tag{40}$$

It can be readily shown that

$$\phi_c = \frac{\mathrm{i}}{\sigma}Ak^2\frac{2\hat{\mu}}{\sqrt{J}}I_0(kr)\exp(\sigma t + \mathrm{i}kz). \tag{41}$$

Thus the pressure correction p_c which is proportional to $J^{-1/2}$ induces a velocity correction proportional to $J^{-1/2}$. This velocity correction gives rise to uncompensated shear stress proportional to J^{-1} which may induce a new pressure correction now proportional to J^{-1}. In this way we may generate, successively, irrotational solutions proportional to increasing powers of $J^{-1/2}$. We believe that only the first pressure correction proportional to $J^{-1/2}$ is of physical significance; the higher order corrections are not considered in the normal stress balance (33).

6. Comparison of the growth rate

We compare the dispersion relation (38) from VCVPF with (24) from VPF, (25) from IPF and (17) from the exact solution. Eqs. (17), (24), (25) and (38) are solved by numerical methods for the growth rate σ and the values of σ are compared.

First we examine two practical cases: 2% PAA in air and 2% PEO in air (following Funada and Joseph [8]). We choose the diameter of the fluid cylinder to be 1 cm. The σ versus k plots for 2% PAA and 2% PEO are shown in Figs. 2 and 3, respectively. These figures show that the results from VCVPF are almost indistinguishable from the exact solution, whereas IPF and VPF overestimates σ significantly.

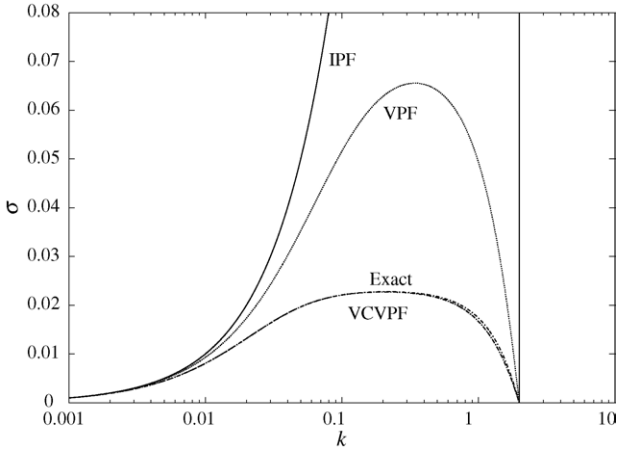

Fig. 2. The growth rate σ vs. k from inviscid potential flow (IPF), viscoelastic potential flow (VPF), viscoelastic correction of VPF (VCVPF) and the exact solution. The growth rates for the exact solution and VCVPF are almost the same. The fluid is 2% PAA, $\rho = 0.99\,\mathrm{g\,cm^{-1}}$, $\mu = 96\,\mathrm{P}$, $\gamma = 45.0\,\mathrm{dyn\,cm^{-1}}$, $\lambda_1 = 0.039\,\mathrm{s}$, $\lambda_2 = 0\,\mathrm{s}$, $J = 4.834 \times 10^{-3}$, $\hat{\lambda}_1 = 0.263$.

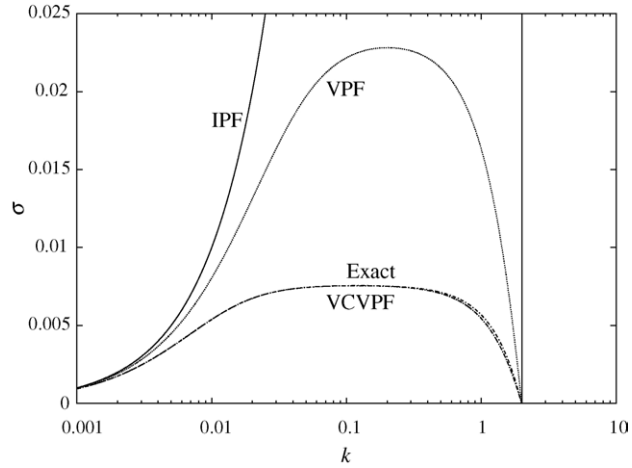

Fig. 3. The growth rate σ vs. k from inviscid potential flow (IPF), viscoelastic potential flow (VPF), viscoelastic correction of VPF (VCVPF) and the exact solution. The results of the exact solution and VCVPF are almost the same. The fluid is 2% PEO, $\rho = 0.99\,\mathrm{g\,cm^{-1}}$, $\mu = 350\,\mathrm{P}$, $\gamma = 63.0\,\mathrm{dyn\,cm^{-1}}$, $\lambda_1 = 0.21\,\mathrm{s}$, $\lambda_2 = 0\,\mathrm{s}$, $J = 5.091 \times 10^{-4}$, $\hat{\lambda}_1 = 1.676$.

Capillary instability is controlled by three dimensionless numbers: J, $\hat{\lambda}_1$, and $\hat{\lambda}_2$. We vary these parameters and present the computed growth rate in Figs. 4–7. The Reynolds number J ranges from 10^{-4} to 10^4, $\hat{\lambda}_1$ ranges from 0.1 to 1000, and $\hat{\lambda}_2$ ranges from 0 to 100. In all the cases, the growth rates from VCVPF are in excellent agreement with the exact solution, indicating that our additional pressure contribution is valid for a wide range of controlling parameters.

Figs. 4 and 5 show that the growth rates increase with $\hat{\lambda}_1$ when J and $\hat{\lambda}_2$ are fixed. Comparing Figs. 5 and 6, it can be seen that the effect of $\hat{\lambda}_2$ is opposite to that of $\hat{\lambda}_1$; the growth rates decreases with $\hat{\lambda}_2$. When $\hat{\lambda}_1 = \hat{\lambda}_2$, the fluid becomes Newtonian. When the Reynolds number is as high as 10^4 (Fig. 7), IPF and VPF slightly over-estimate the maximum growth rate whereas the VCVPF results are almost the same as the exact solution.

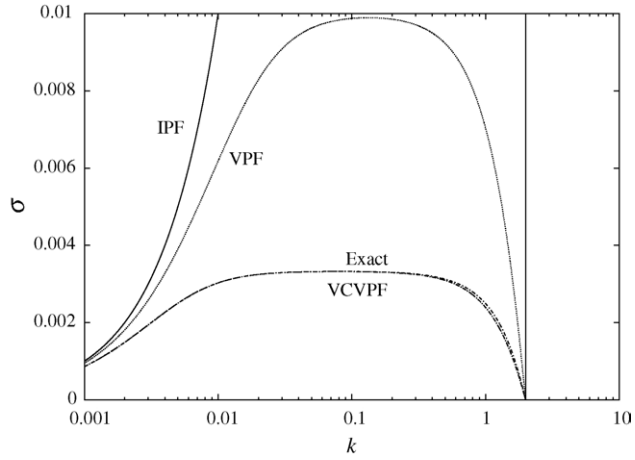

Fig. 4. The growth rate σ vs. k from inviscid potential flow (IPF), viscoelastic potential flow (VPF), viscoelastic correction of VPF (VCVPF) the exact solution. $J = 10^{-4}$, $\hat{\lambda}_1 = 0.1$, $\hat{\lambda}_2 = 0$.

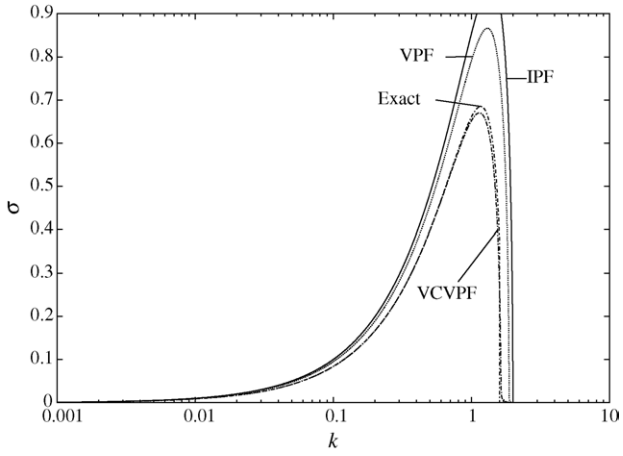

Fig. 5. The growth rate σ vs. k from inviscid potential flow (IPF), viscoelastic potential flow (VPF), viscoelastic correction of VPF (VCVPF) and the exact solution. $J = 10^{-4}$, $\hat{\lambda}_1 = 1000$, $\hat{\lambda}_2 = 0$.

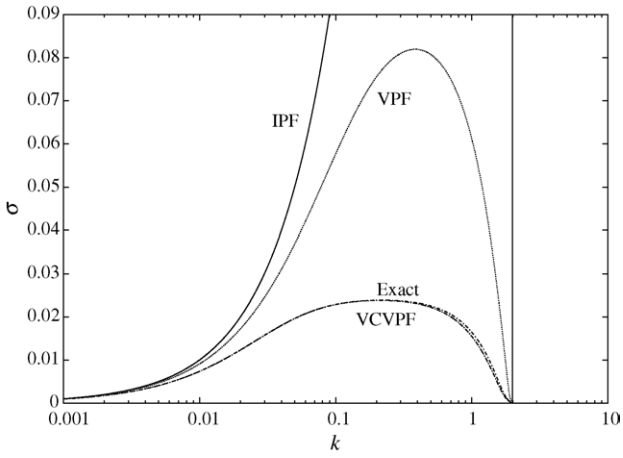

Fig. 6. The growth rate σ vs. k from inviscid potential flow (IPF), viscoelastic potential flow (VPF), viscoelastic correction of VPF (VCVPF) and the exact solution. $J = 10^{-4}$, $\hat{\lambda}_1 = 1000$, $\hat{\lambda}_2 = 100$.

In Table 1 we present the maximum growth rate σ_m and the associated wave number k_m computed from VPF, VCVPF and the exact solution. The value of σ_m given by VPF is several times larger than the exact result when J is small. VCVPF gives excellent approximation to the values of σ_m and k_m in all the cases.

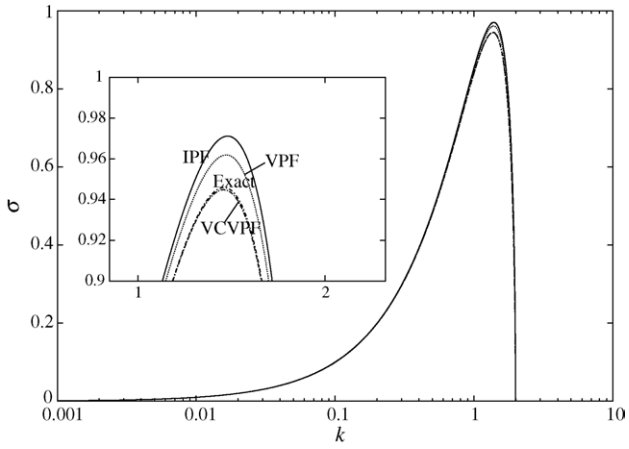

Fig. 7. The growth rate σ vs. k from inviscid potential flow (IPF), viscoelastic potential flow (VPF), viscoelastic correction of VPF (VCVPF) and the exact solution. $J = 10^4$, $\hat{\lambda}_1 = 0.1$, $\hat{\lambda}_2 = 0$. When the Reynolds number J is large, viscoelastic effects are relatively small, and the four curves are close; but differences among them can be seen near the peak growth rate. The inset is the amplified plot for the region near the peak growth rate. VCVPF is the best approximation to the exact solution.

7. Comparison of the stream function

Next we compare the stream functions from VPF, VCVPF and the exact solution at the same wave number. The wave number chosen for the comparison is k_m at which the maximum growth rate σ_m occurs in the exact solution. The relation between the constants A_1 and A_2 in the exact stream function (15) and A in the potential flow solution (22) must be established before one can compare the stream functions. Here this relation is obtained by assuming that the magnitude of the disturbance H is the same in the exact solution and in the potential flow solution.

We use a superscript 'E' for quantities appearing in the exact solution and (15) and (16) are rewritten as

$$\psi^E = [A_1^E r I_1(kr) + A_2^E r I_1(k_v r)] \exp(\sigma^E t + ikz), \tag{42}$$

$$\eta^E = H^E \exp(\sigma^E t + ikz). \tag{43}$$

Table 1
Maximum growth rate σ_m and the associated wave number k_m for viscoelastic potential flow (VPF), viscoelastic correction of VPF (VCVPF) and the exact solution in Figs. 2–7

Figure	VPF		VCVPF		Exact solution	
	k_m	σ_m	k_m	σ_m	k_m	σ_m
2	3.439e−01	6.557e−02	2.052e−01	2.274e−02	2.135e−01	2.278e−02
3	2.025e−01	2.283e−02	1.183e−01	7.554e−03	1.229e−01	7.559e−03
4	1.331e−01	9.899e−03	7.831e−02	3.322e−03	8.154e−02	3.323e−03
5	1.309e+00	8.665e−01	1.144e+00	6.703e−01	1.170e+00	6.850e−01
6	3.848e−01	8.200e−02	2.101e−01	2.384e−02	2.186e−01	2.390e−02
7	1.386e+00	9.618e−01	1.374e+00	9.447e−01	1.375e+00	9.458e−01

For inviscid potential flow (IPF) solution, $k_m = 1.394$ and $\sigma_m = 0.9711$ in all the six cases.

Table 2
The growth rate σ computed from viscoelastic potential flow (VPF), viscoelastic correction of VPF (VCVPF) and the exact solution at the same wave number k_m

J	$\hat{\lambda}_1$	$\hat{\lambda}_2$	k_m	σ^{VPF}	σ^{VCVPF}	σ^{E}
4.834×10^{-3}	0.263	0	0.2135	0.06345	0.02274	0.02278
5.091×10^{-4}	1.676	0	0.1229	0.02252	0.007554	0.007559
10^{-4}	0.1	0	0.08154	0.009843	0.003322	0.003323
10^{-4}	1000	0	1.170	0.8495	0.6696	0.6850
10^{-4}	1000	100	0.2186	0.07718	0.02384	0.02390
10^{4}	0.1	0	1.375	0.9617	0.9447	0.9458

In the exact solution, k_m is the wave number for the maximum growth rate.

The relation between A_1^E and A_2^E is determined by the zero-shear-stress condition at $r \approx R$:

$$A_2^E = \frac{-2k^2 I_1(kR)}{(k^2+k_v^2)I_1(k_v R)} A_1^E. \tag{44}$$

Therefore, we can write the stream function as

$$\psi^E = A_1^E r\left[I_1(kr) - \frac{2k^2 I_1(kR)}{(k^2+k_v^2)I_1(k_v R)} I_1(k_v r)\right] \times \exp(\sigma^E t + \mathrm{i}kz). \tag{45}$$

The amplitude of the disturbance H^E is related to A_1^E through the kinematic condition:

$$H^E = \frac{\mathrm{i}k}{\sigma^E}\left(1 - \frac{2k^2}{k^2+k_v^2}\right) I_1(kR) A_1^E. \tag{46}$$

Now we consider the potential flow solution which is indicated by a superscript 'P'. The stream function and the disturbance are given by

$$\psi^P = A^P r I_1(kr)\exp(\sigma^P t + \mathrm{i}kz), \tag{47}$$

$$\eta^P = H^P \exp(\sigma^P t + \mathrm{i}kz), \tag{48}$$

respectively. The amplitude of the disturbance H^P is related to A^P through the kinematic condition:

$$H^P = \frac{\mathrm{i}k}{\sigma^P} A^P I_1(kR). \tag{49}$$

We assume that the amplitude of the disturbance is the same in the exact solution and the potential flow solution. Thus $H^E = H^P$ and it follows that

$$A^P = A_1^E \frac{\sigma^P}{\sigma^E}\left(1 - \frac{2k^2}{k^2+k_v^2}\right). \tag{50}$$

Then the stream function of the potential flow can be written as

$$\psi^P = A_1^E \frac{\sigma^P}{\sigma^E}\left(1 - \frac{2k^2}{k^2+k_v^2}\right) r I_1(kr)\exp(\sigma^P t + \mathrm{i}kz). \tag{51}$$

Now we can compare (45) and (51). The stream function is decomposed into two parts, the exponential function depending on t and z and the rest part depending on r. Since we are comparing the stream functions at the same wave number k_m, the comparison of the exponential function is equivalent to the comparison of the growth rate. In Table 2, we list the values of the growth rate σ computed from VPF, VCVPF and the exact solution. In all the cases, the growth rate from VPF is larger than the exact result, whereas the growth rate from VCVPF is very close to the exact result. The rest part of the stream function depends on r and we define

$$\mathrm{SF}(r) = \frac{\sigma^{VPF}}{\sigma^E}\left(1 - \frac{2k^2}{k^2+k_v^2}\right) r I_1(kr) \quad \text{for VPF;} \tag{52}$$

$$\mathrm{SF}(r) = \frac{\sigma^{VCVPF}}{\sigma^E}\left(1 - \frac{2k^2}{k^2+k_v^2}\right) r I_1(kr) \quad \text{for VCVPF;} \tag{53}$$

$$\mathrm{SF}(r) = r\left[I_1(kr) - \frac{2k^2 I_1(kR)}{(k^2+k_v^2)I_1(k_v R)} I_1(k_v r)\right] \quad \text{for the exact solution.} \tag{54}$$

Three examples for the comparison of the function SF(r) are shown in Figs. 8–10. The curves for SF(r) are very close to straight lines, indicating power functions. This can also be

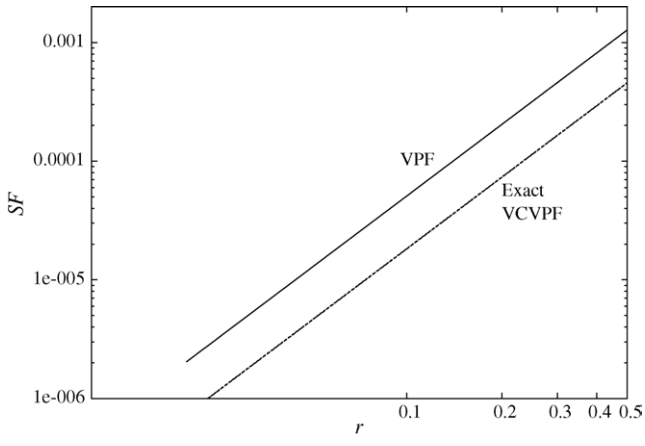

Fig. 8. The part of the stream function depending on r defined in (52)–(54) for viscoelastic potential flow (VPF), viscoelastic correction of VPF (VCVPF) and the exact solution respectively. The fluid is 2% PAA, $J = 4.834\times10^{-3}$, $\hat{\lambda}_1 = 0.263$, $\hat{\lambda}_2 = 0$. The wave number for the maximum growth rate $k_m = 0.2135$ is chosen for the comparison.

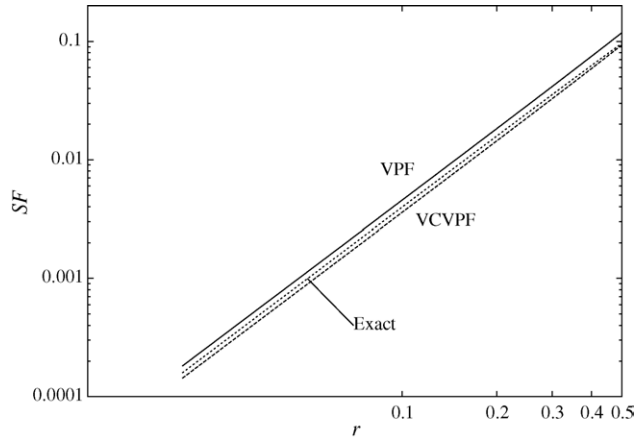

Fig. 9. The part of the stream function depending on r defined in (52)–(54) for viscoelastic potential flow (VPF), viscoelastic correction of VPF (VCVPF) and the exact solution respectively. In this case, $J = 10^{-4}$, $\hat{\lambda}_1 = 1000$, $\hat{\lambda}_2 = 0$. The wave number for the maximum growth rate $k_m = 1.170$ is chosen for the comparison.

seen from (52)–(54). The expansion of the modified Bessel function gives

$$I_1(kr) = \frac{kr}{2} + \frac{k^3 r^3}{16} + \frac{k^5 r^5}{384} + \mathrm{O}(r^7). \tag{55}$$

Higher order terms of r may be neglected because $0 \le r \le 0.5$ inside the cylinder. If we only keep the first term in the expansion, the stream functions (52) and (53) become, respectively

$$\mathrm{SF}(r) = \frac{\sigma^{\mathrm{VPF}}}{\sigma^{\mathrm{E}}}\left(1 - \frac{2k^2}{k^2 + k_v^2}\right)\frac{kr^2}{2} + \mathrm{O}(r^4) \quad \text{for VPF;} \tag{56}$$

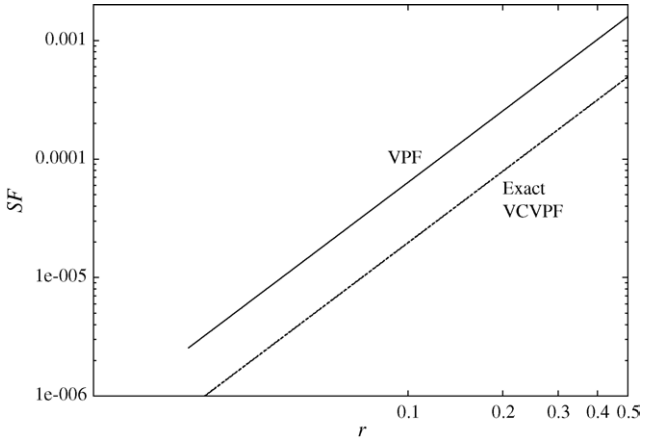

Fig. 10. The part of the stream function depending on r defined in (52)–(54) for viscoelastic potential flow (VPF), viscoelastic correction of VPF (VCVPF) and the exact solution respectively. In this case, $J = 10^{-4}$, $\hat{\lambda}_1 = 1000$, $\hat{\lambda}_2 = 100$. The wave number for the maximum growth rate $k_m = 0.2186$ is chosen for the comparison.

$$\mathrm{SF}(r) = \frac{\sigma^{\mathrm{VCVPF}}}{\sigma^{\mathrm{E}}}\left(1 - \frac{2k^2}{k^2 + k_v^2}\right)\frac{kr^2}{2} + \mathrm{O}(r^4)$$
for VCVPF. (57)

For (54), we also expand $I_1(kR)$ and $I_1(k_v R)$ and keep only the leading term, which gives rise to

$$\mathrm{SF}(r) = \frac{kr^2}{2} - \frac{2k^2(kR/2)}{(k^2 + k_v^2)(k_v R/2)}\frac{k_v r^2}{2} + \mathrm{O}(r^4)$$
$$= \left(1 - \frac{2k^2}{k^2 + k_v^2}\right)\frac{kr^2}{2} + \mathrm{O}(r^4)$$
for the exact solution. (58)

Eqs. (56)–(58) show that the functions SF(r) are approximately quadratic functions for small r and this is confirmed in Figs. 8–10. The comparison of the leading terms of SF(r) depends directly on the growth rate σ^{VPF}, σ^{VCVPF} and σ^{E}. Since $\sigma^{\mathrm{VPF}} > \sigma^{\mathrm{E}}$, the curves for SF($r$) of VPF are higher than those for the exact solution. On the other hand, σ^{VCVPF} is very close to σ^{E} and the curves for VCVPF and the exact solution almost overlap. Combining the comparison of the growth rate in Table 2 and the comparison of the function SF(r) in Figs. 8–10, we show that the stream function given by VCVPF is in remarkably good agreement with the exact solution. This result indicates that the vorticity plays a small role in the exact solution and our VCVPF solution, which is based solely on potential flow, can give an excellent approximation to the flow.

8. Discussion

Chang et al. [12] did a long wave study of the stretching dynamics of bead-string filaments for FENE and Oldroyd-B fluids. They also did a long wave study of linear stability and their results can be compared to ours. To this end, we first convert the parameters used by Chang et al. to the parameters used by us. In the notation of Chang et al. *Ca* is the capillary number, *We* is the Weissenberg number and *S* is the retardation number. We linearize the stress equation of Chang et al. and reduce it to a form comparable to our Jeffreys model (3), then the relation between *We* and *S* used by Chang et al. and $\hat{\lambda}_1$ and $\hat{\lambda}_2$ used by us is revealed. After taking the different length and time scales into account, we can express the parameters in Chang et al. in terms of our parameters

$$Ca = \frac{2}{J}, \quad We = \frac{4\hat{\lambda}_1}{\sqrt{J}}, \quad \text{and} \quad S = \frac{\hat{\lambda}_2}{\hat{\lambda}_1}. \tag{59}$$

Then the dispersion relation given by the linear stability analysis of Chang et al. (their Eq. (16)) can be written as

$$\hat{\lambda}_1\sigma^3 + \left(1 + 3k^2\frac{\hat{\lambda}_2}{\sqrt{J}}\right)\sigma^2 + \left[\frac{3k^2}{\sqrt{J}} - \frac{k^2\hat{\lambda}_1}{4}(4 - k^2)\right]\sigma$$
$$- \frac{k^2}{4}(4 - k^2) = 0. \tag{60}$$

Now we consider the dispersion relation (38) from the VCVPF method. The dimensionless radius $R = 1/2$ and the Bessel functions can be expanded for small k

$$\frac{I_0(kR)}{I_1(kR)} = \frac{4}{k} + \frac{k}{8} - \frac{k^3}{768} + \mathrm{O}(k^5),$$
$$\frac{2I_0(kR)}{I_1(kR)} - \frac{1}{kR} = \frac{6}{k} + \frac{k}{4} - \frac{k^3}{384} + \mathrm{O}(k^5). \quad (61)$$

Inserting (61) into (38), we can obtain

$$\left(1 + \frac{k^2}{32}\right)\hat{\lambda}_1\sigma^3 + \left[1 + \frac{k^2}{32} + 3k^2\frac{\hat{\lambda}_2}{\sqrt{J}}\left(1 + \frac{k^2}{24}\right)\right]\sigma^2 + \left[\frac{3k^2}{\sqrt{J}}\left(1 + \frac{k^2}{24}\right) - \frac{k^2\hat{\lambda}_1}{4}(4 - k^2)\right]\sigma - \frac{k^2}{4}(4 - k^2) + \mathrm{O}(k^4) = 0. \quad (62)$$

The expansion of the Bessel functions can also be applied to the exact solution and the result will be compared to (60) and (62). After some arrangement, the dispersion relation (17) of the exact solution can be written as

$$\frac{4k^3k_v}{\sqrt{J}}\hat{\mu}\left[\frac{I_0(k_vR)}{I_1(k_vR)} - \frac{1}{k_vR}\right] - \frac{2k^2(k^2 + k_v^2)}{\sqrt{J}}\hat{\mu} \times \left[\frac{I_0(kR)}{I_1(kR)} - \frac{1}{kR}\right] - \frac{2k^3}{\sigma}\left(\frac{1}{R^2} - k^2\right) + (k^2 + k_v^2)\frac{k}{\sigma}\left(\frac{1}{R^2} - k^2\right) - (k^2 + k_v^2)\sigma\frac{I_0(kR)}{I_1(kR)} = 0. \quad (63)$$

After expanding the Bessel functions as power series of k, we obtain

$$\hat{\lambda}_1\left(1 + \frac{k^2}{32}\right)\sigma^3 + \left(1 + \frac{k^2}{32} + 3k^2\frac{\hat{\lambda}_2}{\sqrt{J}}\right)\sigma^2 + \left[\frac{3k^2}{\sqrt{J}} - \frac{k^2\hat{\lambda}_1}{4}(4 - k^2)\right]\sigma - \frac{k^2}{4}(4 - k^2) + \mathrm{O}(k^4) = 0. \quad (64)$$

The dispersion relation (64) given by the exact solution is different from both (60) given by Chang et al. and (62) given by our VCVPF method; the first order differences are $\mathrm{O}(k^2)$ in both cases. The differences between (64) and (60) are two $k^2/32$ terms in the coefficients of σ^3 and σ^2; the differences between (64) and (62) are two $k^2/24$ terms in the coefficients of σ^2 and σ.

The limit of a Newtonian fluid can be obtained by letting $\hat{\lambda}_1 = \hat{\lambda}_2 = 0$. Then the dispersion relations (60), (62) and (64) reduce to, respectively

$$\sigma^2 + \frac{3k^2}{\sqrt{J}}\sigma - \frac{k^2}{4}(4 - k^2) = 0 \quad \text{for Chang et al.}; \quad (65)$$

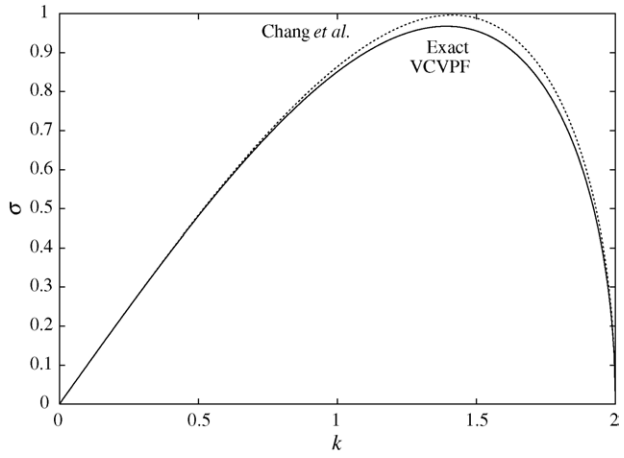

Fig. 11. The growth rate σ as a function of k computed using (60) given by Chang et al., (38) given by our VCVPF method, and (17) given by the exact solution. The fluid is water with $\rho = 1000\,\mathrm{kg/m^3}$, $\mu = 0.001\,\mathrm{kg/(m\,s)}$, $\gamma = 0.0728\,\mathrm{N/m}$. The diameter of the liquid cylinder is assumed to be 0.01 m and the Reynolds number is $J = 7.28 \times 10^5$.

$$\left(1 + \frac{k^2}{32}\right)\sigma^2 + \frac{3k^2}{\sqrt{J}}\left(1 + \frac{k^2}{24}\right)\sigma - \frac{k^2}{4}(4 - k^2) + \mathrm{O}(k^4) = 0 \quad \text{for VCVPF}; \quad (66)$$

$$\left(1 + \frac{k^2}{32}\right)\sigma^2 + \frac{3k^2}{\sqrt{J}}\sigma - \frac{k^2}{4}(4 - k^2) + \mathrm{O}(k^4) = 0 \quad \text{for the exact solution.} \quad (67)$$

The first order differences among the dispersion relations (65)–(67) are $\mathrm{O}(k^2)$. The difference between (65) and (67) is a $k^2/32$ term in the coefficient of σ^2; the difference between (66) and (67) is a $k^2/24$ term in the coefficient of σ.

In Figs. 11–15, we plot the growth rate σ as a function of k computed using (60) given by Chang et al., (38) given by our

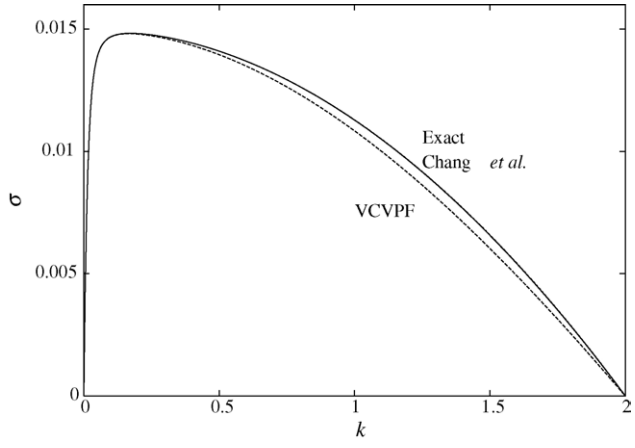

Fig. 12. The growth rate σ as a function of k computed using (60) given by Chang et al., (38) given by our VCVPF method, and (17) given by the exact solution. The fluid is a Newtonian fluid SO10000 oil with $\rho = 969\,\mathrm{kg/m^3}$, $\mu = 10\,\mathrm{kg/(m\,s)}$, $\gamma = 0.021\,\mathrm{N/m}$. The Reynolds number is $J = 2.04 \times 10^{-3}$.

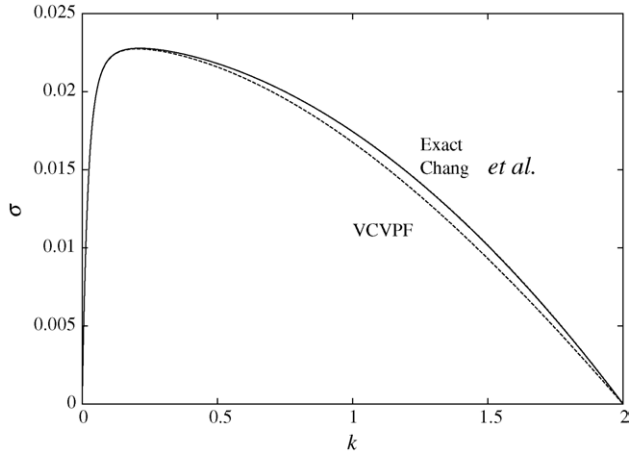

Fig. 13. The growth rate σ as a function of k computed using (60) given by Chang et al., (38) given by our VCVPF method, and (17) given by the exact solution. The fluid is 2% PAA with $J = 4.834 \times 10^{-3}$, $\hat{\lambda}_1 = 0.263$, $\hat{\lambda}_2 = 0$.

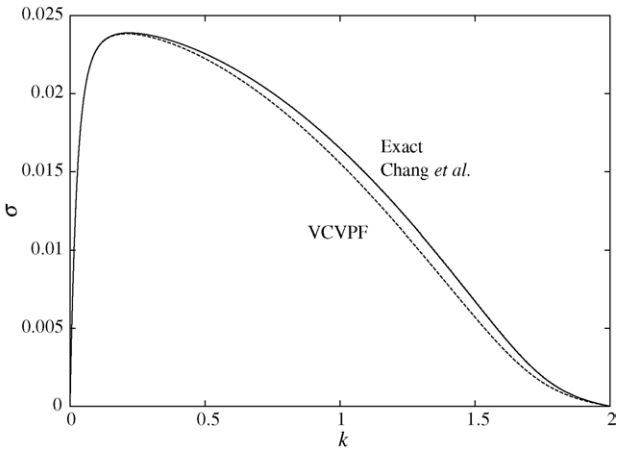

Fig. 15. The growth rate σ as a function of k computed using (60) given by Chang et al., (38) given by our VCVPF method, and (17) given by the exact solution. The fluid is a viscoelastic fluid with $J = 10^{-4}$, $\hat{\lambda}_1 = 1000$, $\hat{\lambda}_2 = 100$.

VCVPF method, and (17) given by the exact solution. Both Newtonian fluids and viscoelastic fluids are compared. The limit of Newtonian fluids is achieved by setting $\hat{\lambda}_1$ and $\hat{\lambda}_2$ to be zero in (60), (38) and (17). There is almost no difference between the three curves when k is close to zero, and small differences can be seen when k is close to 2. The dispersion relation of Chang et al. is in better agreement with the exact solution when the Reynolds number J is small (Figs. 12–15), whereas our VCVPF is in better agreement with the exact solution when J is large (Fig. 11).

In this work, linear stability analysis of the capillary instability of a viscoelastic thread is carried out under the assumption that the flow is irrotational. The non-zero irrotational shear stress at the surface of the liquid thread does not agree with the zero-shear-stress condition. We derive a pressure contribution in addition to the irrotational pressure. This additional pressure contribution depends on the viscoelastic parameters and cancels out the power due to the uncompensated irrotational shear stress in the energy equation. We include the additional pressure contribution, the irrotational pressure and the extra stress evaluated using the irrotational flow in the normal stress balance at the surface, then a dispersion relation is obtained. We call this approach as the viscoelastic correction of the viscoelastic potential flow (VCVPF). The comparison of the growth rate and the stream function show that the VCVPF solution is an excellent approximation to the exact solution. The dispersion relation given by VCVPF is also compared to that obtained by Chang et al. [12] using a long wave approximation. The differences between the two dispersion relations are negligible when the wave number k is small and both dispersion relations are in remarkably good agreement with the exact solution.

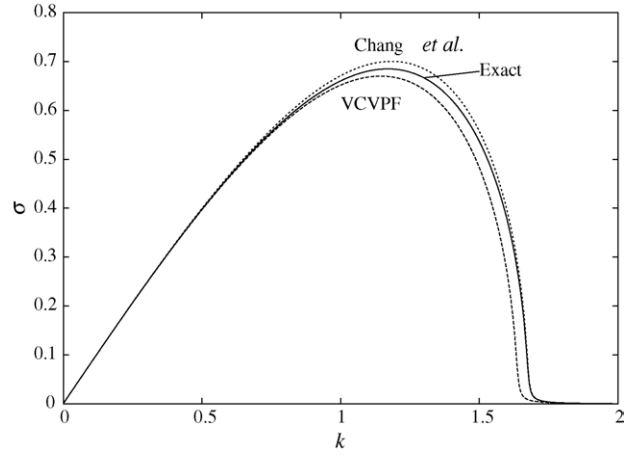

Fig. 14. The growth rate σ as a function of k computed using (60) given by Chang et al., (38) given by our VCVPF method, and (17) given by the exact solution. The fluid is a viscoelastic fluid with $J = 10^{-4}$, $\hat{\lambda}_1 = 1000$, $\hat{\lambda}_2 = 0$.

Acknowledgement

This work was supported in part by the NSF under grants from Chemical Transport Systems.

References

[1] L. Rayleigh, On the capillary phenomena of jets, Proc. R. Soc. London A 29 (1879) 71.
[2] J.A.F. Plateau, Statique experimentale et theorique des liquide soumis aux seules forces moleculaire, vol. ii, 1873, p. 231.
[3] S. Tomotika, On the instability of a cylindrical thread of a viscous liquid surrounded by another viscous fluid, Proc. R. Soc. London A 150 (1935) 322.
[4] S. Middleman, Stability of a viscoelastic jet, Chem. Eng. Sci. 20 (1965) 1937.
[5] M. Goldin, J. Yerushalmi, R. Pfeffer, R. Shinnar, Breakup of a laminar capillary jet of a viscoelastic fluid, J. Fluid Mech. 38 (1969) 689.

[6] S.L. Goren, M. Gottlieb, Surface-tension-driven breakup of viscoelstic liquid threads, J. Fluid Mech. 120 (1982) 245.
[7] T. Funada, D.D. Joseph, Viscous potential flow analysis of capillary instability, Int. J. Multiphase Flow 28 (2002) 1459.
[8] T. Funada, D.D. Joseph, Viscoelastic potential flow analysis of capillary instability, J. Non-Newtonian Fluid Mech. 111 (2003) 87.
[9] D.D. Joseph, J. Wang, The dissipation approximation and viscous potential flow, J. Fluid Mech. 505 (2004) 365.
[10] J. Wang, D.D. Joseph, T. Funada, Pressure correction for potential flow analysis of capillary instability of viscous fluids, J. Fluid Mech. 522 (2005) 383.
[11] V.M. Entov, On the stability of capillary jets of elastoviscous fluids, J. Eng. Phys. Thermophys. 34 (1978) 243.
[12] H.-C. Chang, E.A. Demekhin, E. Kalaidin, Iterated stretching of viscoelastic jets, Phys. Fluids 11 (1999) 1717.